


Angular-Asymmetric Transmitting Metasurface and Splitter for Acoustic Waves: Combining the Coherent Perfect Absorber and a Laser

Shuting Cao and Zhilin Hou*

School of Physics and Optoelectronics, South China University of Technology, Guangzhou 510640, China

 (Received 27 August 2019; revised manuscript received 31 October 2019; published 6 December 2019)

The coherent perfect absorber (CPA) and laser are a pair of inversely worked wave structures that satisfy the time-reversal relation. We point out that, if the wave energy absorbed by the CPA can be recovered and then be reemitted by its corresponding laser, the combination of CPA and laser will be a wave-controlling device that can “move” the wave energy from one place to another. By extending the concepts of the CPA and laser from previously studied one-dimensional non-Hermitian systems to the two-dimensional ones, this understanding is used to simplify the design of the metasurface in this paper. As examples, an angular-asymmetric transmitting metasurface and wave splitter, which act as a perfect transmitter and retroreflector for waves coming from two oppositely tilted angles and splitting an incident wave into two directions with arbitrary amplitude ratio and phase difference, respectively, are constructed by combining two pieces of the separately designed CPAs. The idea not only greatly simplifies the design of a metasurface, but also bridges between research into the metasurface and a non-Hermitian system.

DOI: [10.1103/PhysRevApplied.12.064016](https://doi.org/10.1103/PhysRevApplied.12.064016)

I. INTRODUCTION

A coherent perfect absorber (CPA) and laser are a special pair of wave devices that satisfy time-reversal symmetry. The relationship between them means that, by replacing the loss (gain) materials by the gain (loss) ones in the CPA (laser), the perfect absorption (lasing) procedure can be attained exactly as the emission (absorption) one [1–10]. This relationship and the underlying physics are suggested to be used in the design of an absorptive interferometer [3,4], perfect wave absorbers in the sub-wavelength region [5,6], light-surface plasma couplers [9], a lens without aberration [11], and others. However, these functional structures are based mostly on the coherent perfect absorption effect, which means that only the procedure of removing the wave energy from space is used, while the antieffect, say the lasing effect, which can bring the wave energy into space is, in fact, seldom used in the design of the structure. We note that, if the wave energy absorbed by the CPA can be recovered and then reemitted by its corresponding lasing structure, a combination of the CPA and laser will act as a special device that can “move” the wave energy from one place to another. This will give an alternative mechanism for a wave-behavior-controlling device.

On the other hand, controlling wave behavior by artificial structures has attracted much attention in recent years. The concept of a metasurface, namely, a two-dimensional (2D) thin artificial structure, was introduced first in an electromagnetic wave system [12] and extended

to an acoustic one [13]. The metasurface provides unique functionalities with a wide potential of engineering applications, such as anomalous refraction and reflection [14–18], asymmetric transmission [19,20], perfect absorption [21,22], retroreflection [23], cloaking [24], and others [25,26]. It is found however that devices for realizing these functionalities are mostly constructed by the phase-gradient approach [17] or its improved approaches [18], which often provide very complicated building subunits. We observe that the design of the metasurface is very similar to the abovementioned CPA-laser pair, if we view it as a structure that can move the wave energy in real space from one part to another or from one channel to another. This similarity and the simple corresponding relationship between the CPA and laser give us an alternative mechanism for the metasurface design.

As a direct application, we show that the abovementioned mechanism can be used to design a transmission-type metasurface. As we know, a transmission-type metasurface is a device designed to transmit an incident wave from the incident side to the transmission side in a designable direction. It is equivalent to a CPA-laser pair because it “absorbs” the wave from the inputting side and “emits” it to the outputting side. This means that the inputting and outputting ends of the metasurface can be separately designed as a CPA and laser. We see that such a separately designed strategy can greatly simplify the design procedure. Here, we take two examples to show the design procedure. As the first example, we show that an angular-asymmetric transmission metasurface (AATM) can be constructed by combining two

*phzlh@scut.edu.cn

pieces of the angular-asymmetric reflective metasurface (AARM). As reported in Ref. [27] for an electromagnetic wave and in Ref. [28] for an acoustic wave, an AARM is a specially designed CPA that can perfectly absorb the waves from a positively tilted incident direction and can, at the same time, perfectly retroreflect the waves from a negatively tilted incident direction. We show that, by combining two pieces of an AARM into a new structure, the combination will have a CPA status at the incident end and a laser status at the outputting end. As a result, an AATM, which acts on both sides as a perfect transmitter and retroreflector for waves coming from two oppositely tilted angles, can be obtained. As the second example, we show that the mechanism can also be used to design a transmitting wave splitter, which is a more general metasurface that can split the plane wave from the $+\alpha$ direction in the inputting side into two plane waves in $\pm\alpha$ directions in the outputting side with arbitrary amplitude ratio and phase differences.

II. NUMERICAL METHOD

We start the design with the AARM. The 2D structure is shown schematically in Fig. 1(a), which is a structured

rigid periodic surface with L - ($L=2$ is shown in the figure) bottomed grooves and one bottomless channel per period. By neglecting wave dissipation in the medium, the bottomed grooves will act as the lossless material with pure imaginary surface impedance at the opening end, while, for the bottomless channel, because reflection from the outgoing end [not shown in Fig. 1(a)] will be smaller than unity, it will act as the loss material with complex surface impedance at the inputting end. The purpose of the design is to find a configuration of the grooves and the channel, so that the surface can act as a CPA when it is illuminated by incident waves from one or two given directions.

Rather than using the phase-graded method suggested in Ref. [28], we introduce here an alternative method based on the general grating theory to design the structure. The alternative method can give a simple structure and clear understanding of the underlying physics. Because of the x -directional periodicity of the structure, the pressure and the y -component particle velocity of the field in the medium above the surface can be written as a summation of the harmonic modes,

$$p = \sum_n A_n^+ e^{-j(k_0 \sin\theta + G_n)x} e^{j k_0 \beta_n y}$$

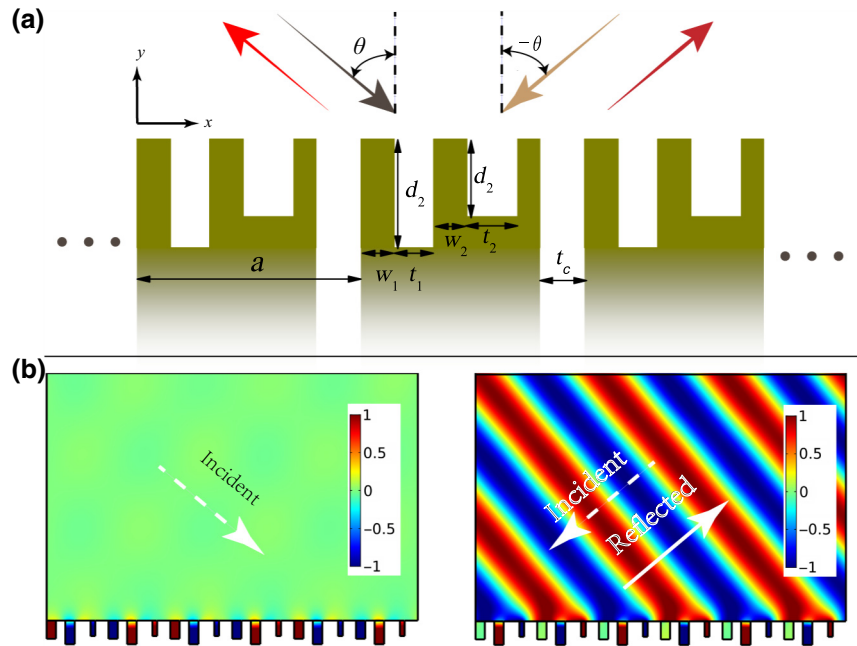


FIG. 1. (a) Schematic illustration of the designed AARM, which is a 2D planar periodic sound-hard surface with bottomed grooves and bottomless channels. The periodicity is along the x direction, and the period is a . One (or two) incident wave from the θ (or $\pm\theta$) direction(s) can be scattered as the diffractive modes. The depth and width of the grooves in each period are denoted as t_l and d_l ($l = 1, 2, \dots, L$), respectively; the width of channel is denoted as t_c ; and the relative distance between the l th and $(l+1)$ th grooves is denoted as w_l . Because reflection from the outgoing end (not shown in the figure) is permitted, the channel will act as the loss material with complex surface impedance at the inputting end. (b) The scattered pressure field distributions for the designed AARM. In which the left and right panels show the results of the incident plane wave from $+50^\circ$ and -50° directions, respectively. The directions of the plane waves are shown by white arrows. Notably, the channels [the $(3l+1)$ th, ($l=0, 1, \dots$) groove in each panel] are replaced by grooves with a depth and impedance calculated by $d_c = \phi_{1c}/2k_0$ and $Z_c = (1 + r_{1c})/(1 - r_{1c})$, respectively.

$$\begin{aligned}
& + \sum_n A_n^- e^{-j(k_0 \sin \theta + G_n)x} e^{-j k_0 \beta_n y} \\
v = & - \frac{1}{Z_0} \sum_n \beta_n A_n^+ e^{-j(k_0 \sin \theta + G_n)x} e^{j k_0 \beta_n y} \\
& + \frac{1}{Z_0} \sum_n \beta_n A_n^- e^{-j(k_0 \sin \theta + G_n)x} e^{-j k_0 \beta_n y}, \quad (1)
\end{aligned}$$

where $k_0 = 2\pi/\lambda_0$ is the wave vector with λ_0 as the working wavelength; θ is the incident angle between the incident ray and the surface normal, which takes a positive (negative) value if the incident ray is at the left (right-) hand side of the surface normal; Z_0 is the characteristic impedance of the medium; A_n^+ and A_n^- are the amplitudes of the n th-order incident and diffractive harmonic modes, respectively; $G_n = (2n\pi/a)$; $n = 0, \pm 1, \dots$ is the Bloch wave vector with a as the period of the structure; and $\beta_n = \pm \sqrt{1 - (\sin \theta + n\lambda_0/a)^2}$ denotes the normalized y -directional propagation constant of the n th-order harmonic mode. It can be seen from Eq. (1) that β_n can be real, i.e., the n th-order diffractive mode is only propagative when the condition $|\sin \theta + n\lambda_0/a| < 1$ is satisfied. By setting $a = \lambda_0/2\sin\alpha$, the system will have only the zero- and negative first-order harmonic modes as the propagating ones, when θ satisfies the condition $2\sin(\alpha-1) < \sin\theta < 4\sin(\alpha-1)$. As we will show in Sec. III, the system is equivalent to a two-port non-Hermitian system under this setting, and the design target is to find the spectrum singularity of the system, at which the incident plane waves with incident angle $\theta = \pm\alpha$ can be perfectly “absorbed.”

On the other hand, the pressure and y -component particle velocity field in the grooves and channel can be expressed as the superposition of the waveguide modes; the field at the inputting end ($y = 0$) of the l th groove (or channel) can be expressed generally as

$$\begin{aligned}
p_l = & \sum_k H_{kl}^+ \cos \frac{(k-1)\pi}{t_l} (x - x_l) \left(1 + \left| \frac{H_{kl}^-}{H_{kl}^+} \right| e^{-j\phi_{kl}} \right) \\
v_l = & - \frac{1}{Z_0} \sum_k H_{kl}^+ \sigma_{kl} \cos \frac{(k-1)\pi}{t_l} (x - x_l) \\
& \times \left(1 - \left| \frac{H_{kl}^-}{H_{kl}^+} \right| e^{-j\phi_{kl}} \right), \quad (2)
\end{aligned}$$

where x_l and t_l are the position and width of the l th groove (or channel), respectively; H_{kl}^+ (H_{kl}^-) ($k = 1, 2, \dots$) is the amplitude of the k th-order waveguide mode propagating into (out from) the l th groove (or channel); ϕ_{kl} is the phase difference between H_{kl}^+ and H_{kl}^- . By defining the normalized propagating constant of the m th-order waveguide mode in the l th groove (or channel) as $\sigma_{kl} = \sqrt{1 - [(k-1)\lambda_0/2t_l]^2}$, $k = 1, 2, \dots$, and defining

the reflection ratio as $r_{kl} = |H_{kl}^-/H_{kl}^+|$, we always have $r_{kl} = 1$ and $\phi_{kl} = k_0 \sigma_{kl} 2d_l$ for bottomed grooves. While, for the bottomless channel, we can introduce energy loss by restricting $r_{kc} < 1$, and thus, hereafter, we use $l = c$ in the subscripts to denote the terms in the channel.

From Eqs. (1), (2) and the continuum boundary condition at the surface, we can obtain a linear equation set for variables A_n^- and H_{kl}^+ under given A_n^+ , a , x_l , t_l , d_l , x_c , t_c , r_{kc} , and ϕ_{kc} . With the linear equation set, we can search the CPA structure with an optimization procedure. The detailed deduction of the linear equation set is presented in Appendix A. In all of our optimization procedures (see Appendix B), we set the width of the channel, t_c , to be $0.15a$, so that only the zero-order waveguide mode ($k = 1$) can propagate in it, which means that, except r_{1c} and ϕ_{1c} , all other r_{kc} and ϕ_{kc} ($k = 2, 3, \dots$) will be set as zero. The position of the channel is set as $x_c = 0$, and the restriction on the depths of grooves is chosen to be as small as possible (restricted to the region $d_l < 0.3\lambda_0$ in calculations). To avoid a structure with extremely thin walls, narrow grooves, or narrow channels, w_l and t_l are restricted to be greater than $0.05a$.

III. RESULTS AND DISCUSSIONS

As the first example, we use this scheme to search for the AARM or the unidirectional CPA that can absorb the plane wave from a single direction with incident angle $\theta = \alpha$. Notably, for a reciprocal two-port system (i.e., metasurface with only zero- and negative first-order possible diffractive modes), the perfect absorption of the wave from the θ direction means also a retroreflection for the wave from the $-\theta$ direction. Through this method, structures with α from 30° to 88° are searched for and found. We find that, for all of these structures, two grooves per period are enough to realize the function. As examples, we choose the structure with $\alpha = 50^\circ$ to show the results. The optimized parameters are obtained as follows: $d_{1,2} = (0.249, 0.163)\lambda_0$, $w_{1,2} = (0.152, 0.256)a$, $t_{1,2} = (0.153, 0.076)a$, $r_{1c} = 0.634$, and $\phi_{1c} = 2.403$. To verify the effect, finite-element simulations based on COMSOL Multiphysics are performed (see Appendix C for details). The scattered pressure field for incident plane waves from $\theta = +50^\circ$ and -50° directions are presented in the left and right panels in Fig. 1(b), respectively. In the simulation, the channels [the $(3l+1)$ th, ($l = 0, 1, \dots$) groove from the left in each panel] are replaced by bottomed grooves with depth $d_c = \phi_{1c}/2k_0 = 0.191\lambda_0$ and with an impedance of $Z_c = Z_0(1+r_{1c})/(1-r_{1c}) = 4.469Z_0$ at the bottom. It can be found from Fig. 1(b) that the maximum amplitude of the reflective wave in the left panel is about 0.025 and in the right panel is about 0.999 under the incident amplitude of unity. This means that the effect of absorbing (retroreflecting) the incident wave from the positive (negative) 50° direction is perfect.

In this obtained unidirectional CPA, if we swap the directions of the waveguide modes in the channel (i.e., H_{1c}^- is now the incident wave and H_{1c}^+ is the reflective wave) and then define the reflection ratio as $r'_{1c} = (|H_{1c}^+|/|H_{1c}^-|) = (1/r_{1c})$, we will have an impedance at the bottom of the channel of $Z'_c = Z_0[(1 + r'_{1c})/(1 - r'_{1c})] = -Z_0[(1 + r_{1c})/(1 - r_{1c})] = -Z_c$, which means the structure turns from loss to gain. This result means that the CPA and its corresponded time-reversal structure, i.e., the laser, are, in fact, the same structure: it works in CPA mode when it is illuminated by the wave from outside of the structure, but in laser mode when it is illuminated by the waveguide mode inside the channel. With this understanding, we can construct the angular-asymmetric refractive metasurface simply by sticking together the CPA and laser substructure back-to-back with connected channels. Notably, because there is only one channel per period, we can combine the substructures in two different ways: stick them directly back-to-back (referred to as D type hereafter) or first rotate one of them by a π angle along the y axes and then stick them back-to-back (referred to as R type hereafter). Also, because the depth of the channel, calculated by $d_c = \phi_{1c}/2k_0$, is usually smaller than the maximum value of the grooves, the total depth of the channel (and the thickness of the metasurface) should be taken as $d_T = 2d_c + \lambda/2$ to avoid overlapping of the grooves in the thickness direction. As we know, according to $Z = [(1 + r_{1c}e^{-j2k_0d_T})/(1 - r_{1c}e^{-j2k_0d_T})]$, a change of $n\lambda/2$ (n is an integer) of d_T would not change the value of the impedance at the opening of the channel. In Fig. 2, the scattered pressure field for the system with $\alpha = 50^\circ$ under the incident wave with $\theta = \alpha$ is shown, in which the results for the D- and R-type structures are shown in the left and right parts, respectively. The thickness of the whole structure is $d_T = 0.882\lambda_0$. It can be seen that the transmission angles for D- and R-type structures are $+50^\circ$ and -50° , respectively, and the amplitude of the transmitted pressure wave is 0.999 under an incident amplitude of unity for both structures, which means that almost perfect transmission is obtained. We do not show the situation for the incident wave from $\theta = -50^\circ$ because it is the same as that shown the right panel of Fig. 1(b). Because of the symmetry and reciprocity of the structure, the situation will be the same when the incident wave is from the lower half of the metasurface, which means it will be retroreflected back when the incident angle is $\theta = -50^\circ$ ($+50^\circ$), while it will be transmitted through when the incident angle is $\theta = 50^\circ$ (-50°) for the D-type (R-type) structure. These results show that an AATM, which acts on both sides as a perfect transmitter and retroreflector for waves coming from two oppositely tilted angles, is obtained. It is necessary to point out that, because extreme structures with thin walls and narrow grooves are avoided in the structure-searching procedure, both of the thermoviscous and wall-deformation effects in our simulation are neglected (a simulation with

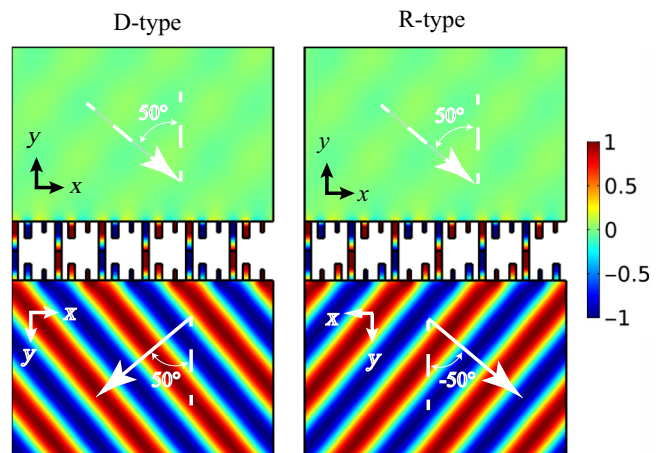


FIG. 2. The scattered pressure field distribution of the designed AATM illuminated by a plane wave from the $+50^\circ$ direction. The left panel is for the D-type structure, and the right panel is for the R-type structure. The white arrows show the directions of the incident and transmitted plane waves. For clarity, the incident fields are not shown. The coordinate systems in each panel are given to show how the AATMs are combined by rotating and sticking the AARMs.

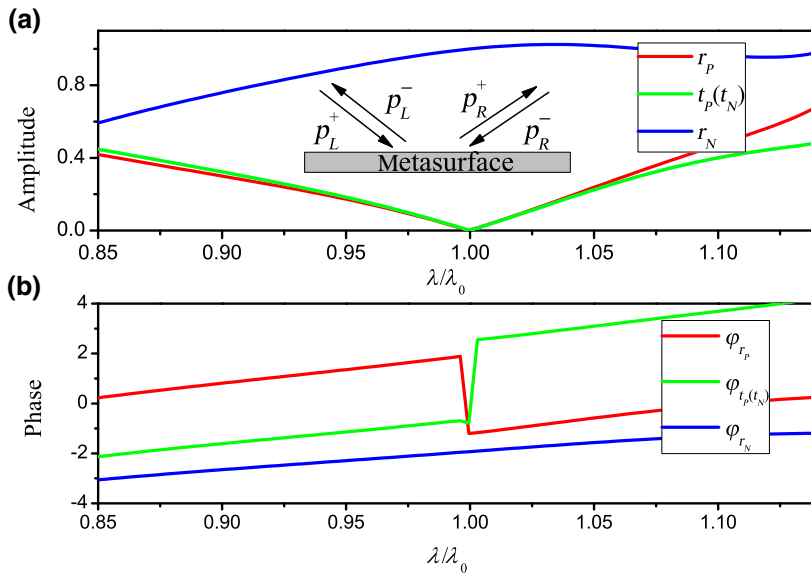
thermoviscous and wall-deformation effects can be found in Appendix D).

The above analysis shows that an AATM can be obtained by combining two pieces of inversely worked CPAs. In the following, we show further that such CPA structures can also be described as a two-port non-Hermitian system; this is a topic that has been attracting much interest in recent years [8,29,30]. One may find that previous works on this topic concentrate mostly on the one-dimensional (1D) system. Here, we show that our 2D case has the same property as that of the 1D one. Such an extension will bridge between research into the metasurface and the non-Hermitian system.

As schematically shown in the inset of Fig. 3(a), by expressing the incoming and outgoing waves from the left- (right-) hand side of the surface-normal directions as $p_L^+(p_R^-)$ and $p_L^-(p_R^+)$, respectively, the scattering property of the metasurface in the upper (or lower) half-infinite space can be described as a scattering matrix,

$$\begin{pmatrix} p_R^+ \\ p_L^- \end{pmatrix} = \begin{pmatrix} t_P & r_N \\ r_P & t_N \end{pmatrix} \begin{pmatrix} p_L^+ \\ p_R^- \end{pmatrix}. \quad (3)$$

We find that the scattering matrix presented in Eq. (3) has only one nonzero element (with $|r_N|=1$) in the angular-asymmetric-reflecting status. This status is also called the spectrum singularity in a non-Hermitian system [6,10]. Analysis of the spectra $|r_P|$, $|t_P|$ (also $|t_N|$), and $|r_N|$, and their phases φ_{r_P} , φ_{t_P} , and φ_{r_N} , as functions of the wavelength, λ , of the incident wave are shown in



Figs. 3(a) and 3(b), in which the singularity at λ_0 can be clearly seen. (Notably, the scattering matrix can also be written in a form with r_P, r_N as diagonal elements, with which the position and property of the exceptional points will be different [31].) Specifically, the phase diagram φ_{r_P} and φ_{t_P} undergo an abrupt π phase shift at λ_0 . This implies the divergence of their derivative with respect to the wavelength, resulting in a diverging delay time of the reflected or transmitted wave [6]. This huge delay time increases the interaction of the waves with the “loss” element, and thus, causes the so-called coherent perfect absorption behavior.

The abovementioned unidirectional CPA is a special case that can only absorb the incident wave from the $+\alpha$ direction; it can be extended to general case, which can perfectly absorb two plane waves from $\pm\alpha$ directions, with arbitrary amplitude ratio and phase differences. For this purpose, we need to set $A_{-1}^+ = 1$, $A_0^+ = Re^{-j\varphi}$, and $A_n^+ = 0 (n \neq 0, 1)$ in Eq. (1), where R and φ are the amplitude ratio and phase difference, respectively, between the zero and -1 modes, and then search for the structure with a target of $A_n^- = 0 (n = 0, \pm 1, \dots)$ (see Appendix B for details). By extension, more complicated functional metasurfaces can be realized.

As our second example, we show that a wave splitter, which can split a plane wave from the α direction into two in-phase plane waves with equal amplitude in $\pm\alpha$ directions, can be designed. To construct such a structure, we need a unidirectional CPA as the inputting end and, at the same time, a general CPA that can absorb perfectly two plane waves from $\pm\alpha$ directions with the same amplitude and phase as the outputting end. Notably, the general CPA in this structure will work in the laser mode, which means it will emit two plane waves in $\pm\alpha$ directions with the same amplitude and phase, according to the time-reversal principle. In Fig. 4, the scattered

FIG. 3. (a) Amplitudes and (b) phases of elements in the scattering matrix as a function of the wavelength of the incident wave. The inset in (a) is given to show that the scattering behavior of the waves in the upper half-infinite space of the AATM can be described as a two-port non-Hermitian system.

pressure field for the structure with $\alpha = 50^\circ$ is shown, in which the wave-splitting phenomenon can be clearly seen. In Fig. 4, we use a Gaussian beam as the incident wave to show intuitively the splitting effect. It is necessary to point out that, to keep the impedance at the opening of the channel unchanged before and after combination, the r_{1c} value for the inputting and outputting ends should be the same. In practice, we can first search the structural parameters $w_l^I, t_l^I, d_l^I, r_{1c}$, and ϕ_{1c}^I for a given t_c for the inputting end. With the obtained r_{1c} and the given t_c , we then search the structural parameters w_l^O, t_l^O, d_l^O , and ϕ_{1c}^O for the outputting end; here, the superscripts “I” and “O” indicate the parameters for the inputting and outputting ends, respectively. Through this method, the thickness of the combined structure can be obtained as $d_T = d_c^I + d_c^O + \lambda/2$, where $d_c^{I(O)}$ is calculated from $\phi_{1c}^{I(O)}/2k_0$. For the structure shown in Fig. 4, we use the same structure as

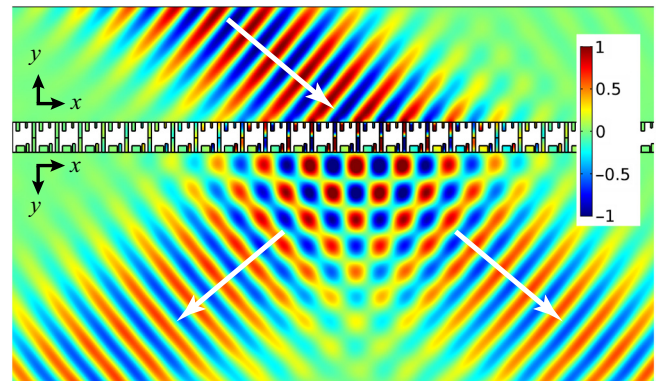


FIG. 4. Pressure field distribution of the wave splitter designed to split the wave from the $+50^\circ$ direction into two in-phase waves with equal amplitude in $\pm 50^\circ$ directions. The white arrows show the incident and transmitted beams.

that given in Fig. 2(b) as the inputting end. Under its r_{1c} and t_c , the structural parameters for the outputting end are $d_{1,2}^O = (0.188, 0.245)\lambda_0$, $w_{1,2}^O = (0.156, 0.063)a$, $t_{1,2}^O = (0.373, 0.121)a$, and $\phi_{1c}^O = 2.009$, and the total thickness of the structure is $d_T = 0.851\lambda_0$.

IV. CONCLUSION

We show that an AATM and a wave splitter can be constructed by combining a CPA and its corresponding laser. Because the inputting and outputting ends are decoupled and separately designed, the suggested mechanism gives a simple design method for a transmission-type metasurface. The scattering property of the structure in the inputting (or outputting) half-infinite space is also studied by the scattering matrix method and found to be as the same as that for the one-dimensional non-Hermitian system. This research not only gives a simple way to design the metasurface, but also bridges between researches into the metasurface and the non-Hermitian system. Recently, a coherent virtual absorption phenomenon was reported in Ref. [32]. It is shown that a virtual wave absorption and reemission phenomenon can also occur in the time domain. With our mechanism and the idea presented in Ref. [32], devices that can control the wave in both real space and the time domain can be expected.

APPENDIX A: DERIVATION OF THE LINEAR EQUATION SET FOR A_n^- AND H_{kl}^+

The continuum condition of the field at the interface can be written as

$$p_s = \begin{cases} p_c & x_c < x < x_c + t_c \\ p_g^l & x_l < x < x_l + t_l \text{ for } l = 1, \dots, L \end{cases}$$

$$v_s = \begin{cases} v_c & x_c < x < x_c + t_c \\ v_g^1 & x_1 < x < x_1 + t_1 \\ \vdots & \vdots \\ v_g^L & x_L < x < x_L + t_L \\ 0 & \text{else,} \end{cases} \quad (\text{A1})$$

where the subscripts “s,” “g,” and “c” of the terms denote the values above, in the grooves, and in the channel, respectively, while the superscript “l” denotes the value in the l th groove.

By substituting Eqs. (1) and (2) into the first term of Eq. (A1), and using the orthogonal relationship of the waveguide modes, we can obtain totally $(L+1) \times M$

equations as

$$\begin{bmatrix} M_1^c \\ M_1^1 \\ \vdots \\ M_1^l \\ \vdots \\ M_1^L \end{bmatrix} (A^+ + A^-) = \begin{bmatrix} M_2^c & 0 & \dots & \dots & \dots & 0 \\ 0 & M_2^1 & 0 & \dots & \dots & \vdots \\ \vdots & 0 & \ddots & 0 & \dots & \vdots \\ \vdots & \dots & 0 & M_2^l & 0 & \vdots \\ \vdots & \dots & \vdots & 0 & \ddots & 0 \\ 0 & \dots & \dots & \dots & 0 & M_2^L \end{bmatrix} \times \begin{bmatrix} H^c \\ H^1 \\ \vdots \\ H^l \\ \vdots \\ H^L \end{bmatrix}, \quad (\text{A2})$$

where $A^{+(-)} = [A_0^{+(-)}, A_{\pm 1}^{+(-)}, \dots, A_{\pm N}^{+(-)}]^T$ and $H^l = [H_{1l}^+, \dots, H_{kl}^+]^T$, ($l = c, 1, \dots, L$) are the column vectors, and the matrixes are defined as

$$M_1^l(k, n) = \frac{1}{t_l} \int_{x_l}^{x_l+t_l} e^{-j(k_0 \sin \theta + G_n)x} \times \cos \left[\frac{(k-1)\pi}{t_l} (x - x_l) \right] dx, \quad (\text{A3})$$

with $l = c, 1, \dots, L$; $n = 0, 1, \dots, N$; and $k = 1, \dots, K$, where N and K are the truncations of the summations in Eqs. (1) and (2), respectively, and

$$M_2^l(k_1, k_2) = (1 + r_{kl} e^{-j\phi_{kl}}) \frac{1}{t_l} \int_{x_l}^{x_l+t_l} \cos \left[\frac{(k_1-1)\pi}{t_l} (x - x_l) \right] \times \cos \left[\frac{(k_2-1)\pi}{t_l} (x - x_l) \right] dx, \quad (\text{A4})$$

with $k_{1,2} = 1, \dots, K$. For grooves with bottoms, $r_{kl} = 1$ and $\phi_{kl} = k_0 \sigma_{kl} 2d_l$, while, for the bottomless channel, we let t_c be a fixed value smaller than that of $\lambda_0/2$, so that both r_{kc} and ϕ_{kc} ($k = 2, 3, \dots$) can be set to zero, except r_{1c} and ϕ_{1c} .

Similarly, by substituting the corresponding y -component velocities into the second term of Eq. (A1), and using the orthogonal relationship of the plane-wave harmonic

modes, we can obtain totally N equations as

$$N_1(A^+ - A^-) = [N_2^c N_2^1 \quad \cdots \quad N_2^l \quad \cdots \quad N_2^L] \begin{bmatrix} H^c \\ H^1 \\ \vdots \\ H^l \\ \vdots \\ H^L \end{bmatrix}, \quad (\text{A5})$$

where

$$N_1(i, j) = \frac{\beta_i}{a} \int_0^a e^{-j(G_i - G_j)x} dx, \quad (\text{A6})$$

with $i, j = 0, \pm 1, \dots, \pm((N-1)/2)$; and

$$N_2^l(j, k) = (1 - r_{kl} e^{-j\phi_{kl}}) \frac{\sigma_{kl}}{a} \int_{x_l}^{x_l+t_l} e^{j(k_0 \sin\theta + G_j)x} \times \cos\left[\frac{(k-1)\pi}{t_l}(x - x_l)\right] dx, \quad (\text{A7})$$

with $j = 0, \pm 1, \dots, \pm((N-1)/2)$ and $k = 1, \dots, K$.

By defining $H = (H^c, H^1, \dots, H^L)^T$, and

$$M_1 = \begin{bmatrix} M_1^c \\ M_1^1 \\ \vdots \\ M_1^l \\ \vdots \\ M_1^L \end{bmatrix}; M_2 = \begin{bmatrix} M_2^c & 0 & \cdots & \cdots & \cdots & 0 \\ 0 & M_2^1 & 0 & \cdots & \cdots & \vdots \\ \vdots & 0 & \ddots & 0 & \cdots & \vdots \\ \vdots & \cdots & 0 & M_2^l & 0 & \vdots \\ \vdots & \cdots & \vdots & 0 & \ddots & 0 \\ 0 & \cdots & \cdots & \cdots & 0 & M_2^L \end{bmatrix}, \quad (\text{A8})$$

$$N_2 = [N_2^c N_2^1 \quad \cdots \quad N_2^l \quad \cdots \quad N_2^L],$$

we can rewrite (A2) and (A5) as

$$M_1(A^+ + A^-) = M_2 H, \quad (\text{A9})$$

and

$$N_1(A^+ - A^-) = N_2 H, \quad (\text{A10})$$

by which we finally get a linear equation set,

$$\begin{pmatrix} -M_1 & M_2 \\ N_1 & N_2 \end{pmatrix} \begin{bmatrix} A^- \\ H \end{bmatrix} = \begin{pmatrix} M_1 \\ N_1 \end{pmatrix} A^+, \quad (\text{A11})$$

with which $(A^-, H)^T$ can be solved by the given A^+ , the structural parameters, and the known values of r_{1c} and ϕ_{1c} .

APPENDIX B: DETAILS OF USING THE GENETIC ALGORITHM TO FIND THE STRUCTURAL PARAMETERS

We use the genetic algorithm to search the structure for the CPA. Before optimization, we set $a = \lambda/2 \sin\alpha$, so that only two possible real diffractive modes along $\pm\alpha$ directions can exist when the incident wave is from the $\theta = +\alpha$ direction. Under this setting, we generally set the incident wave as $(0, \dots, 0, A_{-1}^+, A_0^+, \dots, 0)^T$, under which the parameters $d_{1,2}$, $w_{1,2}$, $t_{1,2}$, r_{1c} , and ϕ_{1c} are searched for the target function $f = [(|A_0^-|^2 + |A_{-1}^-|^2)/(|A_0^+|^2 + |A_{-1}^+|^2)] \rightarrow 0$. For AARM, we need to set $A_{-1}^+ = 0, A_0^+ = 1$, while for the general CPA, which can perfectly absorb two plane waves from $\pm\alpha$ directions with amplitude ratio R and phase difference φ . We need to set $A_{-1}^+ = 1$ and $A_0^+ = R e^{-j\varphi}$.

APPENDIX C: DETAIL SETTING IN NUMERICAL SIMULATION

The two-dimensional full-wave simulations based on finite-element analysis are performed using the COMSOL Multiphysics Pressure Acoustics module. Based on the huge difference between the acoustic characteristic impedances for solid and air, the walls of the channel and grooves are approximated to be sound-hard boundaries in all simulations. For Figs. 1(b), 1(c), and 2, the perfectly matched layers (PMLs) with a thickness of $2a$ are added at the top regions (and bottom regions for Fig. 2; this is not shown in the figure) to reduce the reflection on the boundaries. The Floquet periodic boundary condition is added on the left and right boundaries. In Fig. 4, the PML with a thickness of $2a$ is added at the bottom region, while the top, left, and right boundaries are all set as the plane-wave radiation boundary.

APPENDIX D: EFFECT OF THERMOVISCIOUS AND WALL-DEFORMATION EFFECTS

Thermoviscosity in narrow regions and deformation of thin walls are the two main effects that can affect the performance of the designed metasurface. In our design, because w_l and t_l are restricted to be greater than $0.05a$, we expect that these two effects can be neglected under a relatively low working frequency. To verify this point, we perform a multiphysics simulation based on the thermoviscous acoustic-solid interaction model supplied by the COMSOL software. In the model, both the thermoviscous and wall-deformation effects are taken into account. In the simulation, the material of the metagrating is chosen to be filled epoxy resin with a Young's modulus of $E = 3.2 \times 10^9$ Pa, a Poisson's ratio of $\nu = 0.35$, and a mass density of 1673 kg/m³, and the working medium is chosen to be air (the build-in parameters in COMSOL are used). Results for the D-type structure with two different working frequencies, $f = 3000$ and 8000 Hz, are shown in Fig. 5 as

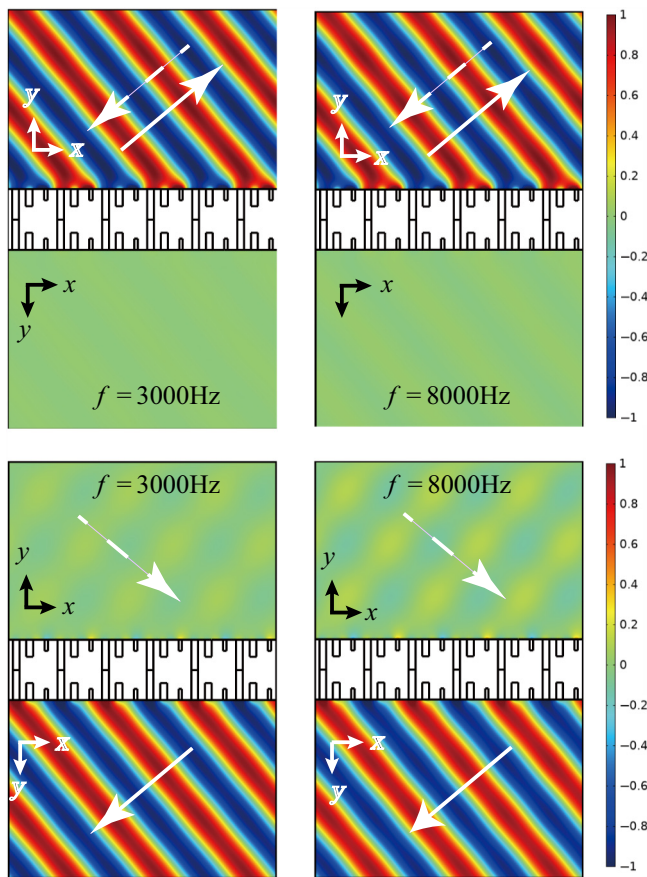


FIG. 5. Scattered pressure field distributions for the D-type structure by the thermoviscous acoustic-solid interaction model under working frequencies of 3000 and 8000 Hz. The material of the metagrating is filled epoxy resin and the working medium is air.

an example. It can be seen that the suggested functionality under both given frequencies is still very clear. In detail, for an incident wave from $+50^\circ$, we can read the amplitude of the transmission wave from 0.97 for $f = 3000$ to 0.95 for $f = 8000$ Hz, while, for the incident wave from -50° , the amplitudes of the retrorefracting wave under both of frequencies are almost unity. This means the thermoviscous and wall-deformation effects can be neglected under $f < 8000$ Hz.

[1] Y. D. Chong, L. Ge, H. Cao, and A. D. Stone, Coherent Perfect Absorbers: Time-Reversed Lasers, *Phys. Rev. Lett.* **105**, 053901 (2010).
 [2] Y. D. Chong, L. Ge, and A. D. Stone, PT-Symmetry Breaking and Laser-Absorber Modes in Optical Scattering Systems, *Phys. Rev. Lett.* **106**, 093902 (2011).
 [3] W. Wan, Y. Chong, L. Ge, H. Noh, A. D. Stone, and H. Cao, Time-reversed lasing and interferometric control of absorption, *Science* **331**, 889 (2011).

[4] A. D. Stone, Gobbling up light with an antilaser, *Phys. Today* **64**, 68 (2011).
 [5] J. Z. Song, P. Bai, Z. H. Hang, and Y. Lai, Acoustic coherent perfect absorbers, *New. J. Phys.* **16**, 033026 (2014).
 [6] R. Hamidreza, E. Yablonovitch, Y. Wang, and X. Zhang, Unidirectional perfect absorber, *IEEE J. Sel. Top. Quant. Electron.* **22**, 5000706 (2016).
 [7] L. Jin and Z. Song, Incident Direction Independent Wave Propagation and Unidirectional Lasing, *Phys. Rev. Lett.* **121**, 073901 (2018).
 [8] V. Achilleos, G. Theocharis, O. Richoux, and V. Pagneux, Non-Hermitian acoustic metamaterials: Role of exceptional points in sound absorption, *Phys. Rev. B* **95**, 144303 (2017).
 [9] H. Noh, Y. Chong, A. D. Stone, and H. Cao, Perfect Coupling of Light to Surface Plasmons by Coherent Absorption, *Phys. Rev. Lett.* **108**, 186805 (2012).
 [10] H. Ramezani, H. K. Li, Y. Wang, and X. Zhang, Unidirectional Spectral Singularities, *Phys. Rev. Lett.* **113**, 263905 (2014).
 [11] F. Monticone, C. A. Valagiannopoulos, and A. Alù, Parity-time symmetric nonlocal metasurfaces: All-angle negative refraction and volumetric imaging, *Phys. Rev. X* **6**, 041018 (2016).
 [12] N. Yu, P. Genevet, M. A. Kats, F. Aieta, J. P. Tetienne, F. Capasso, and Z. Gaburro, Light propagation with phase discontinuities: Generalized laws of reflection and refraction, *Science* **334**, 333 (2011).
 [13] B. Assouar, B. Liang, Y. Wu, Y. Li, J.-C. Cheng, and Y. Jing, Acoustic metasurfaces, *Nat. Rev. Mater.* **3**, 460 (2018).
 [14] A. Diaz-Rubio, J. Li, C. Shen, S. A. Cummer, and S. A. Tretyakov, Power flow-conformal metamirrors for engineering wave reflections, *Sci. Adv.* **5**, eaau7288 (2019).
 [15] A. Diaz-Rubio and S. A. Tretyakov, Acoustic metasurfaces for scattering-free anomalous reflection and refraction, *Phys. Rev. B* **96**, 125409 (2017).
 [16] Y. Fu, C. Shen, Y. Cao, L. Gao, H. Chen, C. T. Chan, S. A. Cummer, and Y. Xu, Reversal of transmission and reflection based on acoustic metagratings with integer parity design, *Nat. Commun.* **10**, 2326 (2019).
 [17] Y. Li, B. Liang, Z. M. Gu, X. Y. Zou, and J. C. Cheng, Reflected wavefront manipulation based on ultrathin planar acoustic metasurfaces, *Sci. Rep.* **3**, 2546 (2013).
 [18] J. Li, C. Shen, A. Díaz-Rubio, S. A. Tretyakov, and S. A. Cummer, Systematic design and experimental demonstration of bianisotropic metasurfaces for scattering-free manipulation of acoustic wavefronts, *Nat. Commun.* **9**, 1342 (2018).
 [19] Y. Li, C. Shen, Y. Xie, J. Li, W. Wang, S. A. Cummer, and Y. Jing, Tunable Asymmetric Transmission via Lossy Acoustic Metasurfaces, *Phys. Rev. Lett.* **119**, 035501 (2017).
 [20] T. Liu, X. Zhu, F. Chen, S. Liang, and J. Zhu, Unidirectional Wave Vector Manipulation in Two-Dimensional Space with an All Passive Acoustic Parity-Time-Symmetric Metamaterials Crystal, *Phys. Rev. Lett.* **120**, 124502 (2018).
 [21] J. Li, W. Wang, Y. Xie, B.-I. Popa, and S. A. Cummer, A sound absorbing metasurface with coupled resonators, *Appl. Phys. Lett.* **109**, 091908 (2016).

- [22] Y. Li and B. M. Assouar, Acoustic metasurface-based perfect absorber with deep subwavelength thickness, *Appl. Phys. Lett.* **108**, 204301 (2016).
- [23] G. Y. Song, Q. Cheng, T. J. Cui, and Y. Jing, Acoustic planar surface retroreflector, *Phys. Rev. Mater.* **2**, 065201 (2018).
- [24] H. Esfahlani, S. Karkar, H. Lissek, and J. R. Mosig, Acoustic carpet cloak based on an ultrathin metasurface, *Phys. Rev. B* **94**, 014302 (2016).
- [25] J. Chen, J. Xiao, D. Lisevych, A. Shakouri, and Z. Fan, Deep-subwavelength control of acoustic waves in an ultracompact metasurface lens, *Nat. Commun.* **9**, 4920 (2018).
- [26] G. Ma, M. Yang, S. Xiao, Z. Yang, and P. Sheng, Acoustic metasurface with hybrid resonances, *Nat. Commun.* **13**, 873 (2014).
- [27] X. Wang, A. Diaz-Rubio, V. S. Asadchy, G. Ptitsyn, A. A. Generalov, J. Ala-Laurinaho, and S. A. Tretyakov, Extreme Asymmetry in Metasurfaces via Evanescent Fields Engineering: Angular-Asymmetric Absorption, *Phys. Rev. Lett.* **121**, 256802 (2018).
- [28] X. Wang, X. Fang, D. Mao, Y. Jing, and Y. Li, Extremely asymmetrical acoustic metasurface mirror at the exceptional point, arXiv e-prints (2019).
- [29] X. Zhu, H. Ramezani, C. Shi, J. Zhu, and X. Zhang, PT-Symmetric Acoustics, *Phys. Rev. X* **4**, 031042 (2014).
- [30] C. Shen, J. Li, X. Peng, and S. A. Cummer, Synthetic exceptional points and unidirectional zero reflection in non-Hermitian acoustic systems, *Phys. Rev. Mater.* **2**, 125203 (2018).
- [31] L. Ge, Y. D. Chong, and A. D. Stone, Conservation relations and anisotropic transmission resonances in one-dimensional PT-symmetric photonic heterostructures, *Phys. Rev. A* **85**, 023802 (2012).
- [32] G. Trainiti, Y. Ra'adi, M. Ruzzene, and A. Alù, Coherent virtual absorption of elastodynamic waves, *Sci. Adv.* **5**, eaaw3255 (2019).